Research Article | Vol. 27, No. 7 | 1 Apr 2019 | OPTICS EXPRESS 9941
Optics EXPRESS

Efficient unidirectional and broadband vertical-emitting optical coupler assisted by aperture-coupled nanopatch antenna array

Y. S. ZENG,[1] S. W. QU,[1,*] C. WANG,[2] B. J. CHEN,[2] AND C. CHAN[2]

[1]*School of Electronic Engineering, University of Electronic Science and Technology of China (UESTC), Chengdu 611731, China*
[2]*State Key Laboratory of Terahertz and Millimeter Waves, Partner Laboratory in City University of Hong Kong, Kowloon, Hong Kong*
**shiweiqu@uestc.edu.cn*

Abstract: Vertical-emitting optical couplers that convert in-plane guided light to out-of-plane emission are crucial elements for future photonic integrated circuits. However, traditional vertical-coupling elements, such as grating couplers, by default radiate light in both upward and downward directions, leading to a significant reduction of device efficiency. In this paper, we propose to solve this problem using a novel nanopatch antenna array, inspired by patch antenna theories commonly deployed in microwave circuits. The proposed nanopatch array features an up-to-down emission directionality up to 12.91 dBc and a wide operating bandwidth of over 400 nm simultaneously. Compared with a typical waveguide grating antenna, our design shows a significantly higher free-space gain of 24.27 dBi. The unidirectional, efficient, and broadband antenna arrays presented here are promising for a range of integrated photonics applications, including inter-chip photonic interconnects, light ranging and detection, optical communications, and biological imaging.

1. Introduction

Photonic integrated circuit (PIC) is a powerful platform that could replace conventional bulk optical systems with scalable, low-cost, highly integrated and high-performance solutions. Such systems are highly promising for future applications ranging from optical interconnects, light ranging and detection, bio-sensing and quantum technologies [1–4]. An essential component in many photonic integrated circuits is the vertical-emitting light couplers, which provide an efficient interface between in-plane guided light waves and out-of-plane emission, either into free space or an optical fiber. The simplest form of vertical couplers is a grating coupler, where a periodically corrugated structure bridges the momentum mismatch between the in-plane and out-of-plane optical modes [5–7]. Such couplers have already enabled a lot of fascinating applications including biosensors [8], on-chip light detection and ranging for future automatic driving [2,9,10] and high-speed optical communications [1]. A major issue associated with grating couplers arises from light being emitted in both upward and downward directions. As a result, the out-coupling efficiency of a typical grating coupler is below 50%, depending on the substrate used, far from the ideally wanted near-unity efficiency [11,12]. As indicated in [11], the power that is emitted down to the substrate side is comparable to that into free space (35% downward versus 50% upward emission). As another example, the emission rates of the grating coupler proposed in [12] are almost identical on both the top and bottom sides. Moreover, after multiple reflections within the substrate, the interference between multiple reflected beams results in undesired blind scanning spots in free space [13], which is highly unfavorable in optical phased array applications.

Nanoantennas, borrowing the ideas from their radio-frequency counterparts, have been intensively explored in the past decade [14,15]. Due to the strong light-matter interaction in these structures and flexible design parameter space, devices based on nanoantennas could be

#356517 https://doi.org/10.1364/OE.27.009941
Journal © 2019 Received 2 Jan 2019; revised 7 Feb 2019; accepted 11 Mar 2019; published 26 Mar 2019

Optics EXPRESS

used to achieve a variety of functionalities within tiny footprints, including nanoscale imaging [16], non-linear signal conversion [17], directional control of light [18] and solar energy harvesting [19]. Just like their radio-frequency counterparts, these nanoantennas at optical frequencies are also ideal candidates for bridging the gap between out-of-plane free-space emission and in-plane guided waves [20–24]. These nanoantenna-based vertical-emitting optical coupler have enabled functionalities including optical beam steering [20] and 3D optical inter-chip interconnections [21]. However, without special engineering, such nanoantennas are also allowed to emit in both directions, resulting in limited overall coupling efficiencies [21,22,25–27] with the maximal coupling efficiency into free space of 46% [21].

To tackle the bidirectional emission issue, several approaches have been proposed. The simplest approach is to place a metallic reflector underneath the coupler structures to break the vertical symmetry and improve out-coupling efficiency. Such strategies have been adopted in both grating couplers [5,28,29] and nanoantennas [20,24]. Unfortunately, the introduction of bottom electrodes is usually not compatible with standard CMOS processes and thus are inconvenient for many PIC applications. Unidirectional emission of light can also be realized by stacking up two waveguide gratings vertically [13]. Although a 93% upward emission ratio is achieved, the required double-layer structure is difficult to fabricate for many photonic platforms and the operating bandwidth is likely limited due to the wavelength-dependent offset length required. In [30], the dimensions of the waveguide grating antenna are optimized for higher upward emissions but the up-to-down emission directionality is no higher than 8.4 dBc and the bandwidth is merely 100 nm.

In this paper, we leverage the concepts of aperture-coupled antennas in microwave engineering to propose a novel nanopatch antenna array for efficient, unidirectional and broadband vertical light emission from PIC platform. The designs presented in this paper are based on a silicon-on-insulator (SOI) platform and are compatible with CMOS technology. The design principles, however, could be readily extended to many other popular photonic platforms (e.g. SiN) that are facing the same challenges. The proposed nanopatch array achieves an up-to-down directionality of up to 12.91 dBc, which is defined as the ratio between upward- and downward-emission optical powers, and an overall coupling efficiency of 71.33%, which is limited by the intrinsic material loss of metal. Moreover, the proposed nanopatch array possesses an 8-dBc up-to-down directionality bandwidth of over 400 nm, significantly higher than the previously reported designs without bottom metal electrodes [13,30]. As a quantitative description of the output power, the gain of the proposed nanopatch array is compared to that of a waveguide grating antenna which is widely adopted in PIC applications. It is demonstrated that the proposed nanopatch array features a gain enhancement of 3.55 dB over the waveguide grating antenna. The fabrication processes of the proposed device are discussed.

2. Design and results

Figures 1(a)-1(c) provides a schematic overview of the proposed structures. The device is based on standard SOI technology but with two additional metallic layers on top. From bottom up, it is composed of a silicon strip waveguide, a silver thin film patterned with rectangular nanoslots, and an array of circular nanopatches. In addition to silver, other metals typically used in CMOS platform, e.g., copper and aluminum [31], can also be applied in the proposed structure. SU-8 photoresist is used between the three layers for separation and planarization purposes. Other commonly used cladding materials in silicon photonics, e.g., SiO_2, can also be used in the proposed structure for separation and planarization. The side view and the cross-section view of the proposed nanopatch array are shown in Figs. 1(b) and 1(c), respectively.

Optics EXPRESS

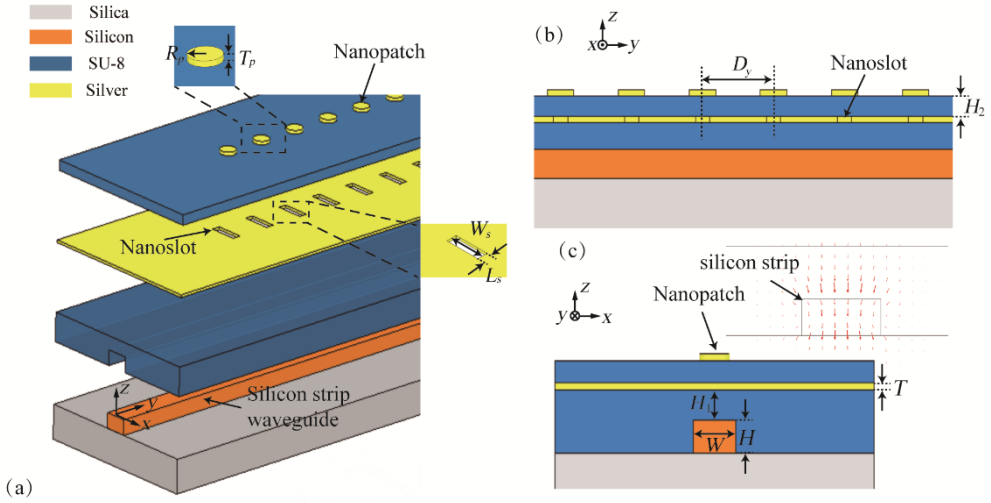

Fig. 1. Structure of the proposed nanopatch array. (a) Illustration of the structure layer by layer. (b) Side view of the device along the *yoz* symmetric plane. (c) Cross-section view of the device. The inset shows the electric field distribution of the waveguide mode at 1550 nm. The parameters are as follows: $W = 0.46$, $H = 0.24$, $H_1 = 0.3$ and $T = 0.08$, all in μm.

The silicon nanostrip, the SU-8 cladding layer and the silver thin film form a hybrid plasmonic waveguide. The electric field distributions of the waveguide mode are shown in the inset of Fig. 1(c). The refractive indices of silicon, SU-8 and silica are 3.48, 1.575 and 1.444, respectively. The permittivity of silver is fitted using Drude model with $\varepsilon_{inf} = 5$, $\omega_p = 13.4 \times 10^{15}$ rad/s and $\Gamma = 1.12 \times 10^{14}$ 1/s. Note that unlike most hybrid plasmonic waveguides reported in the literature, where the ultrathin low-index gap layer usually results in high optical losses [32,33], the proposed design here features a relatively large gap of over 0.2 μm. As a result, light is not strongly confined within the gap and the propagation loss can be reduced significantly. For instance, for an antenna total length of 200 μm, the propagation loss of the waveguide is 2.817 dB for a 0.3 μm gap size. Although the hybrid plasmonic supports a relatively low-loss waveguide mode, the device total length is still limited by plasmonic loss, which is a common issue confronted with plasmonic devices.

Plasmonic nanopatch antennas, with their unique abilities to tailor the emission pattern of light, have been investigated for a variety of applications ranging from polarization conversion [34] to single-photon emission [35,36]. Based on the cavity model, analytical formulations and numerical studies of nanopatch antennas are developed to provide a physical insight into their operating mechanisms [37,38].

In this work, the nanopatch antennas are coupled with the hybrid plasmonic waveguide via the nanoslots etched on the silver thin film. The electric field distributions of the hybrid plasmonic waveguide on the *yoz* plane without and with nanoslots on the silver thin film are shown in Figs. 2(a) and 2(b), respectively. The introduction of the nanoslot imposes perturbations on the original waveguide mode and the electric fields induced within the nanoslot area are mostly polarized along the *y* direction so that the current continuity principle can be maintained. By engineering the nanoslot dimensions, the induced electric fields within the nanoslot equivalently act as driving source and are used to excite the fundamental mode of the nanopatch. For demonstration purpose, a nanopatch element with a slot-etched silver thin film is studied. In the simulation, a voltage driving source is placed on the top of the nanoslot aperture to excite the nanopatch. The model of the single element simulation is shown in Fig. 2(c) and the location of the voltage driving source sheet is marked in Fig. 2(d). The corresponding field distributions are shown in Fig. 2(d). The inset in Fig. 2(d) shows the *z*-component distributions of the electric fields, i.e., E_z on the lower surface of the nanopatch.

Optics EXPRESS

The field distributions in Fig. 2(d) clearly indicate that the existence of the cavity mode formed by the nanopatch and the silver thin film, and that the E_z distribution below the nanopatch coincides with that of the fundamental mode [38].

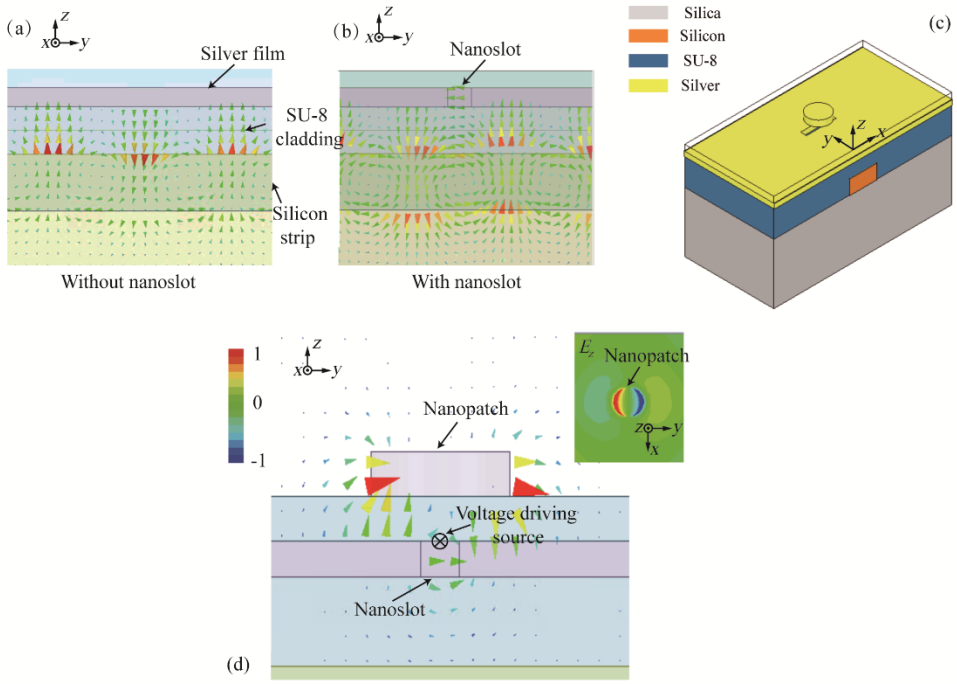

Fig. 2. (a) and (b). Electric field distributions of the hybrid plasmonic waveguide on the *yoz* plane with (b) and without (a) the nanoslot. The parameters are as follows: $W = 0.46$, $H = 0.24$, $T = 0.08$, $W_s = 0.4$, $L_s = 0.1$ and $H_1 = 0.2$, all in μm. (c) Models used for single element simulation. The dimensions of the waveguide are the same as those in (b) and the other parameters are as follows: $R_p = 0.18$, $H_2 = 0.1$ and $T_p = 0.1$, all in μm. The SU-8 substrate between the nanopatch and the silver thin film is set to be transparent to clearly show the nanoslot. (d) Electric field distributions on the *yoz* plane for the model in (c). The inset shows the E_z distribution on the bottom surface of the nanopatch. In the simulation, a voltage driving source is placed on the top of the nanoslot to excite the nanopatch. The wavelength is 1550 nm.

The simulated light emission profiles show clear evidence of unidirectional emission from the designed structures. Figures 3(a) and 3(b) show the *y*- and *z*- component distributions of the electric fields, i.e., E_y and E_z, on the *yoz* plane of the proposed nanopatch array with 15 elements along the *y*-axis, respectively. In the simulation, TM polarized light is launched into the waveguide from the + *y* direction and a wave port is added to excite the hybrid plasmonic waveguide. TM polarized light is used to excite the proposed device throughout this paper. Considering the practical fabrication process of the device, the nanoslots are also filled with SU-8 in the simulation. The near-field distributions in Figs. 3(a) and 3(b) clearly show the couplings between the hybrid plasmonic waveguide and the nanopatches via the nanoslot apertures. As seen in Figs. 3(a) and 3(b), E_z is confined within the cavity formed by the nanopatch and the silver thin film while E_y directly contributes to the light emission. Moreover, the interference between the emitted light of the nanopatch array forms a clear wave front into upper half space, while in the lower half space this behavior is not observed. The device up-to-down directionality, defined as the ratio between the power integral in the upper half space and that in the lower half space, is calculated to be 12.22 dBc. The

Optics EXPRESS

unidirectional light emission is further confirmed by the corresponding far-field emission pattern in Fig. 3(c). The main lobe in free space is 15 dB larger than that in the substrate side.

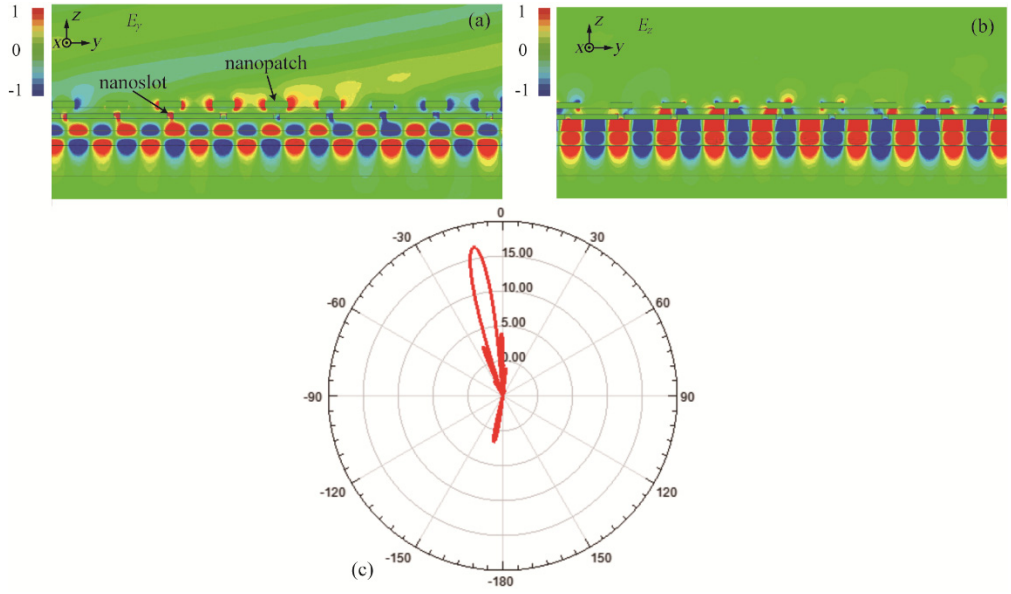

Fig. 3. (a) and (b) E_y and E_z distributions on the *yoz* plane of the proposed nanopatch array with 15 elements along *y*-axis, at the wavelength of 1550 nm. The parameters are as follows: W = 0.46, H = 0.24, T = 0.08,H_1 = 0.2, W_s = 0.4, L_s = H_2 = T_p = 0.1 and D_y = 0.85, all in μm. (c) Corresponding Far-field emission pattern on the *yoz* plane. In the simulation, light is launched into the waveguide from + *y* direction, i.e., the right side, and a wave port is added to excite the hybrid plasmonic waveguide.

The asymmetry introduced by the nanopatches are the key to achieve unidirectional light emissions. Figures 4(a)-4(c) compares the results of the nanopatch antenna array in Fig. 3 and a nanoslot antenna array which has all the parameters remaining the same as those in Fig. 3 but with nanopatches removed. A bidirectional light emission behavior is observed in the nanoslot array case. Due to the bidirectional light emission, the far-field gain of the nanoslot array in free space experiences a drop of roughly 3.86 dB (from 16.67 dBi to 12.81 dBi) compared to that of the nanopatch antenna array (Fig. 4(b)). The gain of an antenna is defined as: $G = 4\pi \dfrac{P(\theta,\varphi)}{P_{accepted}} = 4\pi \dfrac{P(\theta,\varphi)}{P_e / \eta} = \eta * D$, where $P(\theta,\varphi)$, $P_{accepted}$, P_e, D and η denote the radiation power density at the specified angle in free space, the accepted power, total radiated power, directivity and radiation efficiency, respectively. It describes the ability of the antenna to convert the input power into the free space light in the specified direction. Moreover, the main lobe in free space of the nanoslot array is almost the same as that in the substrate side. The near-field distributions of the antenna elements in the nanoslot array case and the nanopatch array case are investigated in detail and shown in Fig. 4(c). In the case of the nanoslot array, the electric fields are mostly distributed within the nanoslot apertures and exhibit a symmetry with respect to the central line of the silver thin film (black dotted line in the left-sided panel of Fig. 4(c)). This explains the bidirectional emission behavior observed in Figs. 4(a) and 4(b). In contrast, in the case of the nanopatch array, instead of being concentrated within the nanoslot, the electric fields are confined within the cavity formed by the nanopatch and the silver thin film, especially around the sharp corners of the nanopatches. The emission pattern of the nanopatch antenna element is a unidirectional one due to the existence of the silver thin film which essentially introduces an image beneath the silver film.

Optics EXPRESS

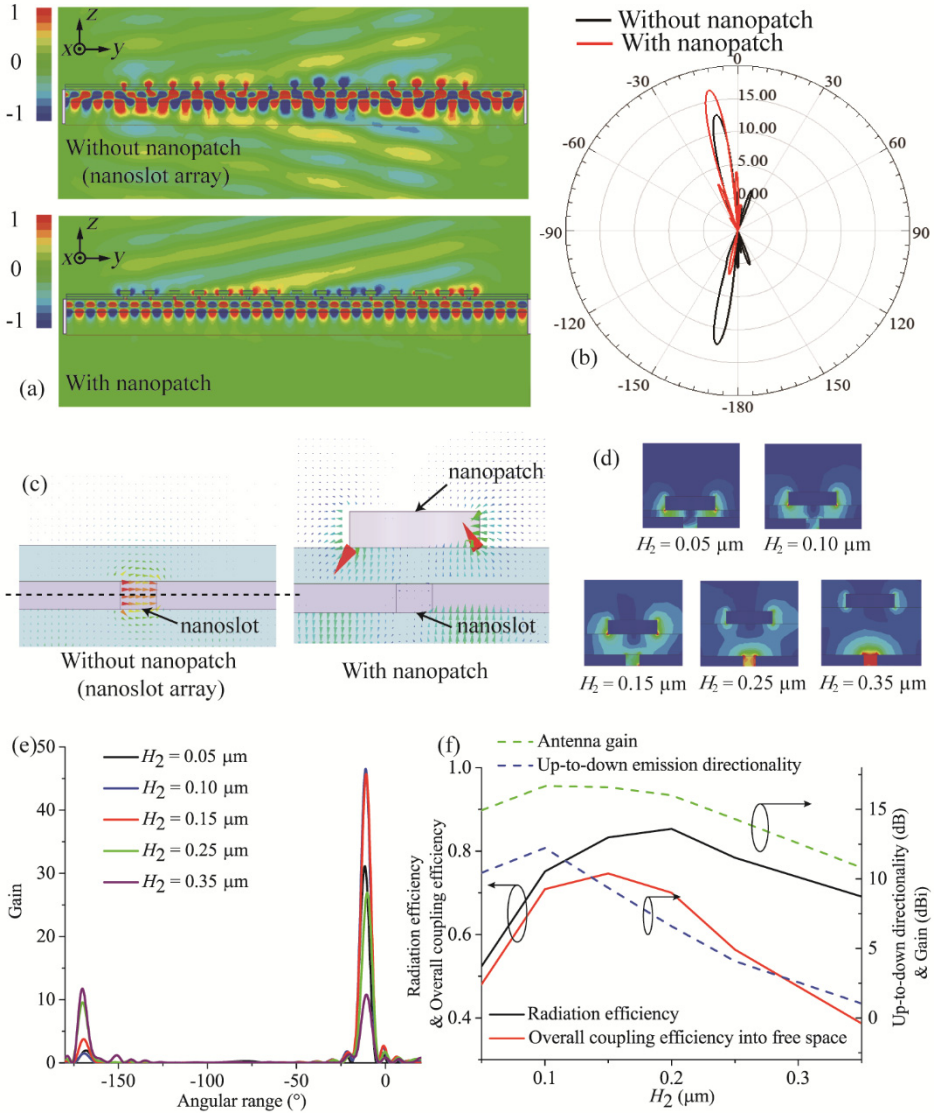

Fig. 4. (a) A comparison of the near-field distributions between the nanopatch array in Fig. 3 (lower-half panel) and a nanoslot antenna array (upper-half panel) which has all the parameters remaining the same as those in Fig. 3 but with all the nanopatches removed. (b) The far-field emission patterns of the nanopatch array and the nanoslot array. (c) Zoom-in view of the electric field distributions of the nanoslot in the nanoslot array (left-sided panel) and the nanopatch in the nanopatch array (right-sided panel). (d) The electric field intensity distributions under different H_2. They are plotted in the same color scale. Other parameters are the same as those in Fig. 3. (e) Far-field gains of the nanopatch array under different H_2. Other parameters are the same as those in Fig. 3. (f) Black solid line: radiation efficiency versus H_2; Red solid line: overall coupling efficiency into free space versus H_2; Blue dashed line: Up-to-down emission directionality versus H_2; Green dashed line: antenna gain versus H_2.

Figures 4(d)-4(e) shows how the modes and the emission patterns change with the variation of the thickness of the SU-8 spacer layer between the nanopatches and the silver film. With the increase of H_2, the intensity of the electric field inside the nanoslot gradually increases and the dominant operating mode gradually changes from the nanopatch mode for H_2 = 0.05 μm to the nanoslot mode for H_2 = 0.35 μm. The up-to-down emission directionality reaches its maximum at H_2 = 0.1 μm and gradually decreases from the 12.22 dB to 1.05 dB

Optics EXPRESS

for H_2 = 0.35 μm, as shown in the blue dash line of Fig. 4(f). A similar trend is also observed in antenna gain, as indicated in the green dash line of Fig. 4(f). Interestingly, although with a higher up-to-down directionality, the antenna gain for H_2 = 0.05 μm is lower than that in the case of H_2 = 0.15 μm. This is because smaller H_1 results in stronger light concentration [39] beneath the nanopatch and the metallic loss increases correspondingly. The radiation efficiency and device overall coupling efficiency into free space are depicted in the black and red solid lines of Fig. 4(f), respectively. As seen from Fig. 4(f), due to metallic loss, the radiation efficiency is merely 52.3% when H_2 = 0.05 μm. The overall coupling efficiency into free space reaches its maximum (75%) at H_2 = 0.15 μm but the up-to-down directionality is not at its maximum. It indicates that there is a tradeoff between the overall coupling efficiency into free space and the up-to-down directionality. A compromise is reached in the case of H_2 = 0.1 μm at which a high up-to-down directionality of 12.22 dB, a gain of 16.67 dBi and a 71% overall coupling efficiency into free space are simultaneously achieved. In the design of photonic circuits, it is a trend to use low-index material like SiO_2 as cladding of the whole device instead of air cladding, which facilitates the designs of many active components like modulators and detectors. The proposed design can be easily adopted to work in that scenario. In that case, the chief design consideration is to adopt proper sizes of the nanopatch antennas because the resonance wavelength of the nanopatch antenna is dependent on the refractive index of the background medium [40].

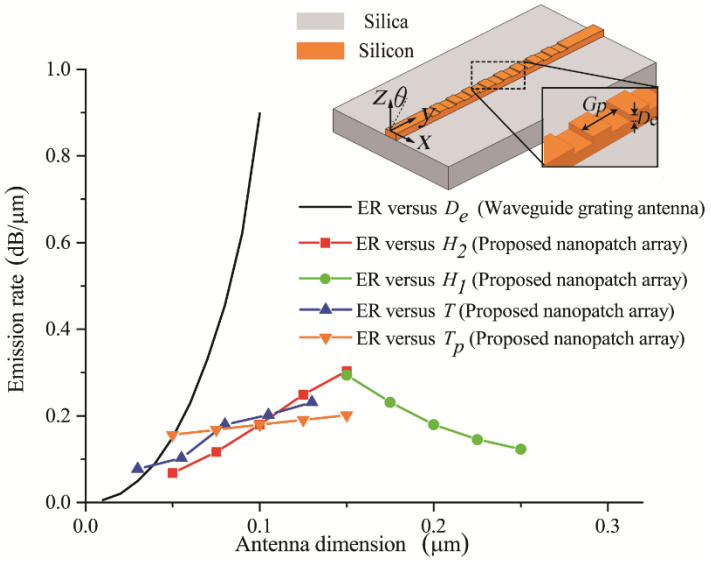

Fig. 5. Dependences of the emission rate (ER) upon antenna dimensions. The black solid line: the emission rate versus D_e of grating antenna; the red solid line with square: the emission rate of nanopatch array versus H_2; the green solid line with circle: the emission rate of nanopatch array versus H_1; the blue solid line with up-triangle: the emission rate of nanopatch array versus T; the orange solid line with down-triangle: the emission rate of nanopatch array versus T_p. Other parameters are the same as those in Fig. 3. For a certain D_e, the emission rate of the waveguide grating antenna is obtained by simulating antennas with different lengths and fitting the relation between antenna length and the remaining power P according to $P = P_0\exp(-2\alpha L)$, where P_0, α, L denote the initial power, emission rate and antenna length, respectively. A 1 μm thick silica cladding is added on top of the waveguide grating antenna to make a fair comparison. The inset shows the structure of the waveguide grating antenna. G_p and D_e represent the grating period and the etching depth, respectively.

Optics EXPRESS

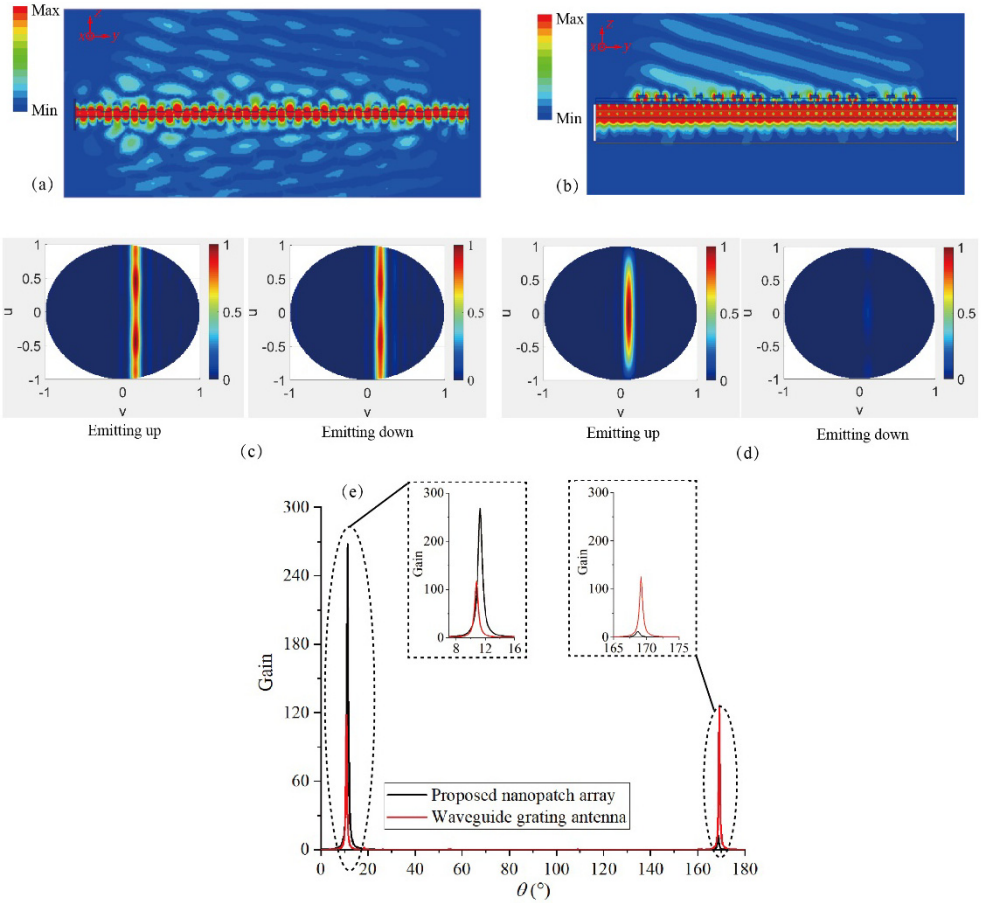

Fig. 6. (a) Near-field distribution on the *yoz* plane of the waveguide grating antenna with D_e = 0.053 μm, G_p = 0.682 μm, D_c = 50% and N_s = 18. The width and height of the silicon strip waveguide are 0.45 and 0.28 μm, respectively. In the simulation, TE polarized light is launched into the waveguide from the -*y* direction. (b) Near-field distribution on the *yoz* plane of the proposed nanopatch array with 15 elements along the *y* direction. The parameters are the same as those in Fig. 3. In the simulation, light is launched from the -*y* direction. (c) and (d) 2-dimensional far-field emission patterns on the upper- and lower-half spaces of the waveguide grating antenna in (a) and the proposed nanopatch array in (b), respectively. (e) Comparisons of the far-field gains on the *yoz* plane of the waveguide grating antenna and the proposed nanopatch array. The parameters of the waveguide grating antenna are as follows: D_e = 0.053 μm, G_p = 0.682 μm, D_c = 50% and N_s = 450. The width and height of the silicon strip waveguide are 0.45 and 0.28 μm, respectively. The parameters of the proposed nanopatch array are the same as those in Fig. 3 but with 353 elements. In the simulation, light is launched from the -*y* direction. The wavelength is 1550 nm.

For further illustrating the advantages of the proposed nanopatch array, a comparison is made against the waveguide grating antenna. The typical structure of the waveguide grating antenna is shown in the inset of Fig. 5, which is formed by etching periodic nanoslots on the silicon strip waveguide. Due to the simple structure and ease of fabrication, waveguide grating antennas have been widely adopted for fiber couplers [5,7,41] and on-chip light emissions [2,9]. However, due to the lack of vertical structural asymmetry, they exhibit almost identical upward and downward light emission strengths [11,12]. In addition, the light emission intensity and the beam direction of the waveguide grating antenna are highly dependent on etching depth and etching period [42]. Figure 5 depicts the emission rates of the waveguide grating antenna versus the etching depth of the grating. In Fig. 5, D_e represents the

Optics EXPRESS

etching depth of the waveguide grating antenna. The emission rates of the proposed nanopatch array under different nanoslot dimensions are also calculated and shown in Fig. 5. For ease of comparison and the sake of brevity, in Fig. 5, the results of both the waveguide grating antenna and the proposed nanopatch array are plotted in the same coordinates. In general, the proposed nanopatch array features a lower emission rate than that of the waveguide grating antenna. A low emission rate results in a large emission aperture which contributes to narrow beam divergence in the far-field and thus is always pursued in optical phased array applications [9,12,42].

The near-field distributions of the waveguide grating antenna and the proposed nanopatch array are compared in Figs. 6(a) and 6(b). The grating period (G_p), number of etched nanoslots (N_s), duty cycle (D_c) and etching depth (D_e) of the waveguide grating antenna are 0.682 μm, 18, 50% and 0.053 μm, respectively. In the simulation, a silica cladding with a thickness of 1 μm is added on top of the waveguide grating antenna because the structure of the proposed nanopatch array contains a SU-8 cladding. For both antennas, light is launched into the waveguide from the -*y* direction. The characteristics of the waveguide grating antenna are very similar under either TE or TM polarization [43,44] while the majority of the research studies on the waveguide grating antenna have been focusing on TE polarization [2,9,12]. Consequently, the TE polarized light is used to excite the waveguide grating antenna in our simulations to make the comparison more convincing. For the waveguide grating antenna, two directional wave fronts are formed with nearly identical intensities going both upwards and downwards. For the proposed nanopatch array, only the upward emission is observed while the downward emission is almost negligible. As a quantitative measure, the up-to-down directionality of the proposed nanopatch array is 12.22 dBc, which is 11.63 dB higher than 0.59 dBc of the waveguide grating antenna. The corresponding far-field emission patterns of both the waveguide grating antenna and the proposed nanopatch array are shown in Figs. 6(c) and 6(d), respectively. As shown in Figs. 6(c) and 6(d), the upward and downward emission patterns of the waveguide grating are very similar while for the proposed nanopatch array, the downward emission is over an order lower than the upward one. Moreover, the far-field emissions of the proposed nanopatch array are more concentrated within an area around the main beam than that of the waveguide grating antenna, which is expected to result in a higher gain at the desired direction. This is because the waveguide grating antenna is essentially a leaky wave antenna and could be considered as a line-source featuring a cone-like 3-dimensional emission pattern which is nearly omnidirectional on the *xoz* cut-plane. For further comparison, the far-field gains of both antennas are calculated and depicted in Fig. 6(e). To make a fair comparison, the proposed nanopatch array and the waveguide grating antenna are compared under similar emission rate and similar beam direction (around 11°). The emission rate of the proposed nanopatch array in Fig. 3 is calculated to be 0.1752 dB/μm and the corresponding etching depth of the waveguide grating antenna with a similar emission rate is 0.053 μm, which is obtained by performing polynomial fitting of the relation between the etching depth and the emission rate in Fig. 5. Note that for an emission rate of 0.1752 dB/μm, the emission length is over 100λ at the wavelength of 1550 nm. It is thus impractical to get the solution to such a large-scale array through full-wave simulations directly. As an alternative, the directivity of the large-scale array can be obtained by the pattern multiplication method and the product of the directivity and the simulated radiation efficiency gives the final gain. Similar strategy is also applied to the waveguide grating antenna. First, a waveguide grating antenna with N_s = 18 is simulated and is considered as the sub-array of the final antenna with N_s = 450. The final radiation pattern is then obtained by the pattern multiplication method. For both antennas, the emission length is set to be 300 μm (only 0.00055% of the input power remains un-emitted), which corresponds to 353 elements for the proposed nanopatch array and 25 sub-arrays for the waveguide grating antenna. As shown in the left-sided inset of Fig. 6(e), the gain of the waveguide grating antenna at the desired beam direction (θ = 10.8°, see the inset of Fig. 5 for the definition of θ) in the free space ($\theta \in$ [-

Optics EXPRESS

90,90]) is 118 while the proposed nanopatch array presents a gain at a similar direction of 267, which is roughly 2.26 times (3.55 dB) higher than that of the waveguide grating antenna. In the substrate side ($\theta \in$ [90,180]∪[-180,-90]), the peak gain of the waveguide grating antenna is even higher than that in the free space (126 versus 118). In contrast, the peak gain of the proposed nanopatch array in the substrate side is only 12, which is over 10 times smaller than that of the waveguide grating antenna, as shown in the right-sided inset of Fig. 6(e). Theoretically, the directivity enhancement in the free space is contributed by the unidirectional light emission (roughly 3 dB) and the dipolar resonance of the nanopatch (2.25 dBic of a dipole), which is 5.25 dBc in total. Here, the calculated directivity enhancement is 4.8 dBc which is close to the 5.25 dBc theoretical value. The 0.45 dB discrepancy could be caused by the errors of the emission rate.

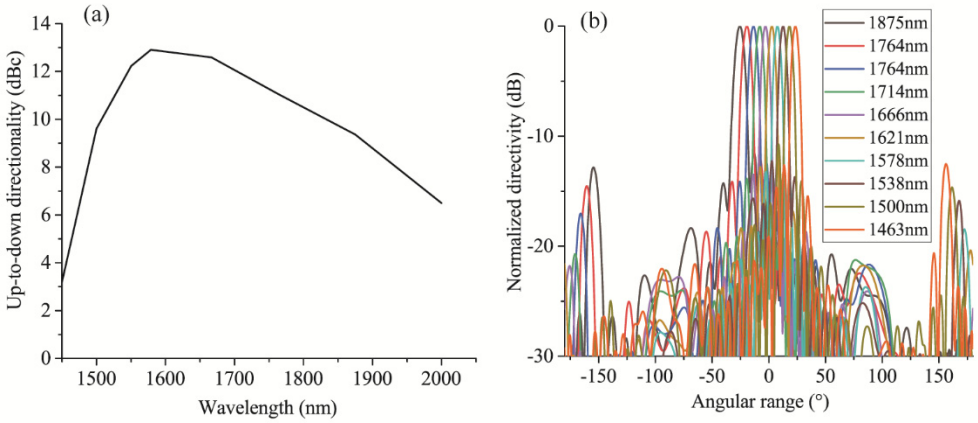

Fig. 7. (a) Up-to-down directionality versus wavelength. The parameters are the same as those in Fig. 3. (b) Normalized far-field directivity patterns at various wavelengths.

Figure 7(a) shows the up-to-down directionality of the proposed nanopatch array versus wavelength. The maximum up-to-down directionality is 12.91 dBc at 1579 nm. The bandwidth within which the up-to-down directionality is above 10 dBc is roughly 280 nm (from 1538 to 1818 nm) and the 8-dBc up-to-down directionality bandwidth is over 400 nm (from 1500 to 1935 nm). The presented bandwidth for unidirectional light emission is significantly higher than the previously reported designs [13,30]. Figure 7(b) shows the normalized emission patterns of the proposed nanopatch array at different wavelengths. The beam can be steered from –23.5° to 25.5° as the wavelength increases from 1463 to 1875 nm. Meanwhile, within the scanning range, the downward emission on the substrate side are at least 12.9 dB lower than the upward emission in free space.

The fabrication tolerances of the proposed nanopatch array are investigated and compared to waveguide grating antennas. Figure 8(a) shows the emission patterns of the waveguide grating antenna in Fig. 6(a) with different D_e. In the simulations, ± 0.05 μm deviations are applied to D_e. As seen from Fig. 8(a), both the beam direction and the gain experience an obvious change versus the variation of D_e. It is because the beam direction of the waveguide grating antenna is determined by the average effective indexes of the etched region and the unetched region [45]. A slight deviation on the etching depth results in a different effective index on the etched region and thus affects the beam direction. In addition, the emission rate of the waveguide grating antenna is also highly dependent on the etching depth [42] and the antenna gain varies accordingly. The dependences of the emission rates on antenna dimensions are compared in Fig. 5. To make a fair comparison, the influences of four vertical dimensions with ± 0.05 μm deviations on the parameters in Fig. 3 are investigated. In Fig. 5,

Optics EXPRESS

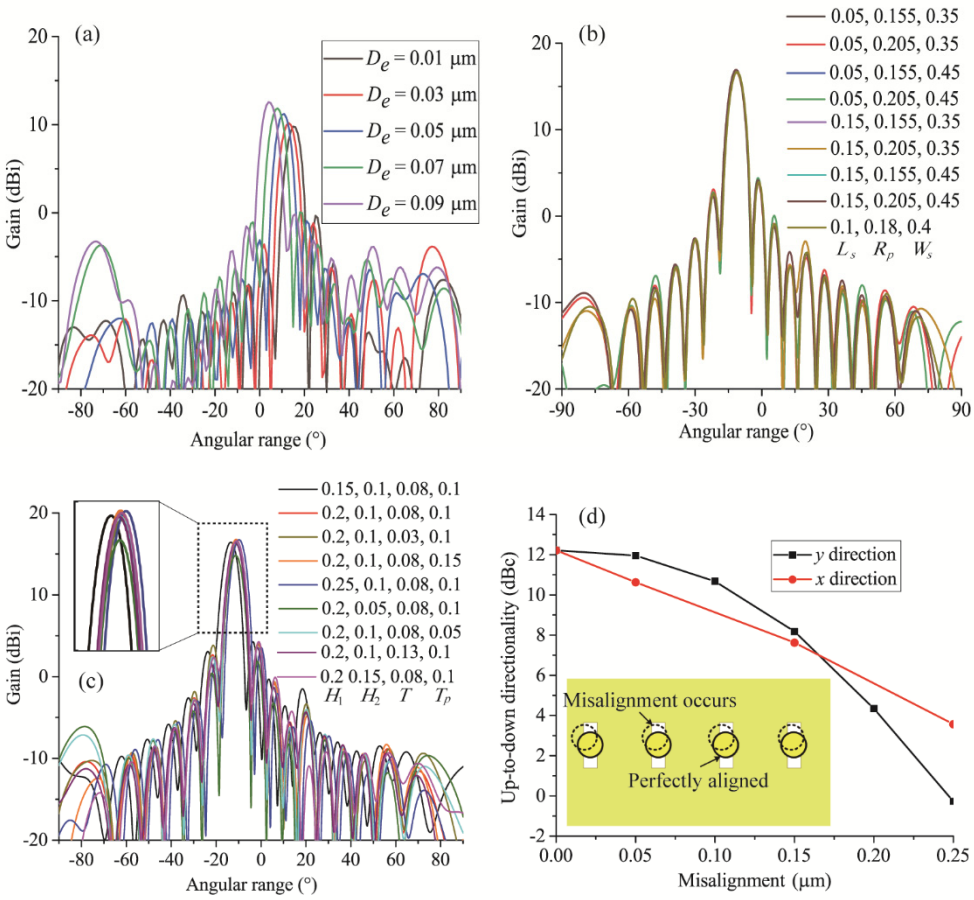

Fig. 8. (a) Far-field gain patterns of the waveguide grating antenna on the *yoz* plane with different D_e. The period of the grating and the duty cycle are 0.68 μm and 50%, respectively. The width and height of the silicon strip waveguide are 0.45 μm and 0.28 μm, respectively. The wavelength is 1550 nm. (b) Far-field gain patterns of the proposed nanopatch array when ± 0.05 μm deviations are applied to the values of W_s, L_s and R_p in Fig. 3. (c) Far-field gain patterns of the proposed nanopatch array when ± 0.05 μm deviations are applied to the values of H_1, H_2, T and T_p in Fig. 3. (d) The influences of the misalignments between the nanopatch layer and the nanoslot layer. Red solid line: up-to-down directionality versus the misalignment along *x* direction. Black solid line: up-to-down directionality versus the misalignment along *y* direction. The inset shows a schematic illustration of the misalignments. The yellow circles denote the positions of the nanopatches with no misalignments and the dotted circles indicate the positions of the nanopatches when misalignments occur. The other parameters are the same as those in Fig. 3.

the red, green, blue and orange lines with symbols plot the dependences of emission rate upon H_2, H_1, T and T_p, respectively. The emission rate of the waveguide grating antenna exhibits a dramatic variation of over 150 times (from 0.00568 dB/μm to 0.89792 dB/μm) when D_e increase from 0.01 μm to 0.1 μm. As a comparison, the largest variation of the emission rate of the proposed nanopatch array within the same ± 0.05 μm deviation is roughly 4.5 times when H_2 increases from 0.05 to 0.15 μm (red solid line with square marker in Fig. 5). Figures 8(b) and 8(c) give the emission patterns of the proposed nanopatch array with various dimension combinations. Both the influences of lateral and vertical dimensions are investigated. In Fig. 8(b), the numbers in the legend denote the values of three lateral-dimension parameters, i.e., L_s, R_p and W_s in μm, respectively. In Fig. 8(c), the numbers in the

Optics EXPRESS

legend denote the values of four vertical-dimension parameters, i.e., H_1, H_2, T and T_p, respectively. In general, the emission patterns are more sensitive to the changes in vertical dimensions than lateral dimensions. With the variations of lateral dimensions, there are only slight differences on the side lobes of the emission patterns while the emission directions, beam widths and the gains are almost unchanged, as observed in Fig. 8(b). For vertical dimensions, the variation of H_2 gives rise to a gain drop (green curve in Fig. 8(c)) and slight beam direction deviations are observed with the variation of H_1 (black and blue curves in Fig. 8(c)). Other parameters only have minor effects. Consistent with the analysis in Fig. 4, H_2 has great influences on the field distributions of nanopatches which in turn affect the gain of the antenna. H_1 determines the excitation phase of each nanopatch by affecting the propagation constant of the hybrid plasmonic waveguide and thus make the beam directions changed. The influences of the misalignments between the nanopatch layer and the nanoslot layer are also investigated and are shown in Fig. 8(d). A schematic illustration of the misalignments is provided in the inset of Fig. 8(d), in which the yellow circles denote the positions of the nanopatches with no misalignments and the dotted circles indicate the positions of the nanopatches when misalignments occur. The red and black solid lines show the up-to-down directionality versus the misalignments along x and y directions, respectively. Taking 8-dBc up-to-down directionality as the criteria, the simulation results indicate that the fabrication tolerances of the misalignments in both directions are both roughly 0.15 μm.

In this work standard electron beam lithography (EBL) and lift-off process can be employed to fabricate the proposed device. The fabrication process is described in detail as follows: Firstly, the silicon nanostrip waveguide can be fabricated by reactive-ion etching (RIE) process using SiO_2 as protective mask. The SiO_2 hard mask can be removed by wet etching in Hydrofluoric acid. Then a SU-8 layer can be spin-coated onto the SOI wafer and fully cured on a hot-plate at 160 ◦ C. The silver background layer can be deposited onto the SU-8 layer by using the thermal evaporator. The nano-patterns can be fabricated on the PMMA film by EBL following by standard developing process. Finally, the nano-silver pattern can be achieved by a lift-off procedure.

3. Conclusion

In this paper, an on-chip plasmonic nanopatch antenna array presenting unidirectional light emission is introduced. With the proposed nanopatch array, an up-to-down directionality of on-chip light emission of over 12 dBc is achieved. Benefiting from the highly directional light emission, a gain improvement of 3.55 dB is demonstrated, as shown by comparing the proposed nanopatch array with a typical waveguide grating antenna. Moreover, the proposed nanopatch array features a large operating bandwidth of over 400 nm for unidirectional emission, which is significantly higher than the other previously reported designs. Importantly, the proposed structure only involves patterning of metal layers on top of standard optical waveguides, therefore is compatible with the CMOS fabrication process and can also be extended to other photonic platforms. The efficient, unidirectional and broadband nanopatch antenna array could provide a practical coupling solution for a lot of PIC applications including on-chip light ranging and detection, optical communications and on-chip fiber couplers.

Funding

National Natural Science Foundation of China (NSFC) (61622104, 61721001).

References

1. K. Wang, A. Nirmalathas, C. Lim, E. Wong, K. Alameh, H. Li, and E. Skafidas, “High-speed indoor optical wireless communication system employing a silicon integrated photonic circuit,” Opt. Lett. **43**(13), 3132–3135 (2018).
2. J. Sun, E. Timurdogan, A. Yaacobi, E. S. Hosseini, and M. R. Watts, “Large-scale nanophotonic phased array,” Nature **493**(7431), 195–199 (2013).

Optics EXPRESS

3. C. García-Meca, S. Lechago, A. Brimont, A. Griol, S. Mas, L. Sánchez, L. Bellieres, N. S. Losilla, and J. Martí, "On-chip wireless silicon photonics: from reconfigurable interconnects to lab-on-chip devices," Light Sci. Appl. **6**(9), e17053 (2017).
4. C. P. Dietrich, A. Fiore, M. G. Thompson, M. Kamp, and S. Höfling, "GaAs integrated quantum photonics: Towards compact and multi-functional quantum photonic integrated circuits," Laser Photonics Rev. **10**(6), 870–894 (2016).
5. D. Taillaert, P. Bienstman, and R. Baets, "Compact efficient broadband grating coupler for silicon-on-insulator waveguides," Opt. Lett. **29**(23), 2749–2751 (2004).
6. D. Taillaert, W. Bogaerts, P. Bienstman, T. F. Krauss, P. Van Daele, I. Moerman, S. Verstuyft, K. De Mesel, and R. Baets, "An out-of-plane grating coupler for efficient butt-coupling between compact planar waveguides and single-mode fibers," IEEE J. Quantum Electron. **38**(7), 949–955 (2002).
7. D. Taillaert, F. Van Laere, M. Ayre, W. Bogaerts, D. Van Thourhout, P. Bienstman, and P. Baets, "Grating couplers for coupling between optical fibers and nanophotonic waveguides," Jpn. J. Appl. Phys. **45**(8A), 6071–6077 (2006).
8. J. Vörös, J. J. Ramsden, G. Csúcs, I. Szendrő, S. M. De Paul, M. Textor, and N. D. Spencer, "Optical grating coupler biosensors," Biomaterials **23**(17), 3699–3710 (2002).
9. D. N. Hutchison, J. Sun, J. K. Doylend, R. Kumar, J. Heck, W. Kim, C. T. Phare, A. Feshali, and H. Rong, "High-resolution aliasing-free optical beam steering," Optica **3**(8), 887–890 (2016).
10. C. V. Poulton, A. Yaacobi, D. B. Cole, M. J. Byrd, M. Raval, D. Vermeulen, and M. R. Watts, "Coherent solid-state LIDAR with silicon photonic optical phased arrays," Opt. Lett. **42**(20), 4091–4094 (2017).
11. J. Sun, E. Timurdogan, A. Yaacobi, Z. Su, E. S. Hosseini, D. B. Cole, and M. R. Watts, "Large-scale silicon photonic circuits for optical phased arrays," IEEE J. Sel. Top. Quantum Electron. **20**(4), 264–278 (2014).
12. K. Shang, C. Qin, Y. Zhang, G. Liu, X. Xiao, S. Feng, and S. J. B. Yoo, "Uniform emission, constant wavevector silicon grating surface emitter for beam steering with ultra-sharp instantaneous field-of-view," Opt. Express **25**(17), 19655–19661 (2017).
13. M. Raval, C. V. Poulton, and M. R. Watts, "Unidirectional waveguide grating antennas with uniform emission for optical phased arrays," Opt. Lett. **42**(13), 2563–2566 (2017).
14. P. Bharadwaj, B. Deutsch, and L. Novotny, "Optical antennas," Adv. Opt. Photonics **1**(3), 438–483 (2009).
15. L. Novotny and N. Van Hulst, "Antennas for light," Nat. Photonics **5**(2), 83–90 (2011).
16. T. H. Taminiau, R. J. Moerland, F. B. Segerink, L. Kuipers, and N. F. van Hulst, "λ/4 resonance of an optical monopole antenna probed by single molecule fluorescence," Nano Lett. **7**(1), 28–33 (2007).
17. M. Danckwerts and L. Novotny, "Optical frequency mixing at coupled gold nanoparticles," Phys. Rev. Lett. **98**(2), 026104 (2007).
18. T. Kosako, Y. Kadoya, and H. F. Hofmann, "Directional control of light by a nano-optical Yagi–Uda antenna," Nat. Photonics **4**(5), 312–315 (2010).
19. H. A. Atwater and A. Polman, "Plasmonics for improved photovoltaic devices," Nat. Mater. **9**(3), 205–213 (2010).
20. S. W. Qu and Z. P. Nie, "Plasmonic nanopatch array for optical integrated circuit applications," Sci. Rep. **3**(1), 3172 (2013).
21. H. Huang, H. Li, W. Li, A. Wu, X. Chen, X. Zhu, Z. Sheng, S. Zou, X. Wang, and F. Gan, "High-efficiency vertical light emission through a compact silicon nanoantenna array," ACS Photonics **3**(3), 324–328 (2016).
22. L. Yousefi and A. C. Foster, "Waveguide-fed optical hybrid plasmonic patch nano-antenna," Opt. Express **20**(16), 18326–18335 (2012).
23. A. Yaacobi and M. R. Watts, "Frequency-chirped subwavelength nanoantennas," Opt. Lett. **37**(23), 4979–4981 (2012).
24. A. Yaacobi, E. Timurdogan, and M. R. Watts, "Vertical emitting aperture nanoantennas," Opt. Lett. **37**(9), 1454–1456 (2012).
25. A. G. Curto, G. Volpe, T. H. Taminiau, M. P. Kreuzer, R. Quidant, and N. F. van Hulst, "Unidirectional emission of a quantum dot coupled to a nanoantenna," Science **329**(5994), 930–933 (2010).
26. M. Peter, A. Hildebrandt, C. Schlickriede, K. Gharib, T. Zentgraf, J. Förstner, and S. Linden, "Directional emission from dielectric leaky-wave nanoantennas," Nano Lett. **17**(7), 4178–4183 (2017).
27. M. Klemm, "Novel directional nanoantennas for single-emitter sources and wireless nano-links," Int. J. Opt. **2012**, 348306 (2012).
28. F. Van Laere, G. Roelkens, M. Ayre, J. Schrauwen, D. Taillaert, D. Van Thourhout, T. F. Krauss, and R. Baets, "Compact and highly efficient grating couplers between optical fiber and nanophotonic waveguides," J. Lightwave Technol. **25**(1), 151–156 (2007).
29. Y. Ding, H. Ou, and C. Peucheret, "Ultrahigh-efficiency apodized grating coupler using fully etched photonic crystals," Opt. Lett. **38**(15), 2732–2734 (2013).
30. K. Han, V. Yurlov, and N. E. Yu, "Highly directional waveguide grating antenna for optical phased array," Curr. Appl. Phys. **18**(7), 824–828 (2018).
31. S. Zhu, T. Y. Liow, G. Q. Lo, and D. L. Kwong, "Silicon-based horizontal nanoplasmonic slot waveguides for on-chip integration," Opt. Express **19**(9), 8888–8902 (2011).
32. Y. Song, J. Wang, M. Yan, and M. Qiu, "Efficient coupling between dielectric and hybrid plasmonic waveguides by multimode interference power splitter," J. Opt. **13**(7), 075002 (2011).

Optics EXPRESS

33. D. C. Zografopoulos, M. A. Swillam, L. A. Shahada, and R. Beccherelli, "Hybrid electro-optic plasmonic modulators based on directional coupler switches," Appl. Phys., A Mater. Sci. Process. **122**(4), 344 (2016).
34. F. Wang, A. Chakrabarty, F. Minkowski, K. Sun, and Q. H. Wei, "Polarization conversion with elliptical patch nanoantennas," Appl. Phys. Lett. **101**(2), 023101 (2012).
35. F. Bigourdan, F. Marquier, J. P. Hugonin, and J. J. Greffet, "Design of highly efficient metallo-dielectric patch antennas for single-photon emission," Opt. Express **22**(3), 2337–2347 (2014).
36. R. Esteban, T. V. Teperik, and J. J. Greffet, "Optical patch antennas for single photon emission using surface plasmon resonances," Phys. Rev. Lett. **104**(2), 026802 (2010).
37. G. S. Unal and M. I. Aksun, "Bridging the gap between RF and optical patch antenna analysis via the cavity model," Sci. Rep. **5**(1), 15941 (2015).
38. F. Minkowski, F. Wang, A. Chakrabarty, and Q. H. Wei, "Resonant cavity modes of circular plasmonic patch nanoantennas," Appl. Phys. Lett. **104**(2), 021111 (2014).
39. J. A. Schuller, E. S. Barnard, W. Cai, Y. C. Jun, J. S. White, and M. L. Brongersma, "Plasmonics for extreme light concentration and manipulation," Nat. Mater. **9**(3), 193–204 (2010).
40. A. K. U. Michel, D. N. Chigrin, T. W. Maß, K. Schönauer, M. Salinga, M. Wuttig, and T. Taubner, "Using low-loss phase-change materials for mid-infrared antenna resonance tuning," Nano Lett. **13**(8), 3470–3475 (2013).
41. X. Chen and H. K. Tsang, "Polarization-independent grating couplers for silicon-on-insulator nanophotonic waveguides," Opt. Lett. **36**(6), 796–798 (2011).
42. M. Zadka, Y. C. Chang, A. Mohanty, C. T. Phare, S. P. Roberts, and M. Lipson, "On-chip platform for a phased array with minimal beam divergence and wide field-of-view," Opt. Express **26**(3), 2528–2534 (2018).
43. X. Chen and H. K. Tsang, "Polarization-independent grating couplers for silicon-on-insulator nanophotonic waveguides," Opt. Lett. **36**(6), 796–798 (2011).
44. G. Dabos, J. Bolten, A. Prinzen, A. L. Giesecke, N. Pleros, and D. Tsiokos, "Perfectly vertical and fully etched SOI grating couplers for TM polarization," Opt. Commun. **350**, 124–127 (2015).
45. D. Kwong, A. Hosseini, J. Covey, X. Xu, Y. Zhang, S. Chakravarty, and R. T. Chen, "Corrugated waveguide-based optical phased array with crosstalk suppression," IEEE Photonics Technol. Lett. **26**(10), 991–994 (2014).